PAPER

Multi-component crystals containing urea: mechanochemical synthesis and characterization by ^{35}Cl solid-state NMR spectroscopy and DFT calculations†

Cameron S. Vojvodin,[ab] Sean T. Holmes,[ab] Lara K. Watanabe, [iD][c]
Jeremy M. Rawson [iD][c] and Robert W. Schurko [iD]*[ab]

Mechanochemical synthesis provides new pathways for the rational design of multi-component crystals (MCCs) involving anionic or cationic components that offer molecular-level architectures unavailable to MCCs comprising strictly neutral components. Structural characterization of the products of mechanochemical syntheses is essential for divining clear relationships between the nature of coformers, milling conditions, reaction mechanisms, and intermolecular bonding. Notably, when powder X-ray diffraction and solid-state NMR (SSNMR) are combined with plane-wave density functional theory (DFT) calculations, they offer opportunities for NMR crystallographic solutions and structural refinements. Herein, we report mechanochemical syntheses of five urea-containing MCCs of the form $NR_4Cl:x$Urea·yH$_2$O (R = H, Et, n-Pr; x = 1, 2, 3; y = 0, 2), which can be made in high yields (> $ca.$ 99%) and great rapidity (<40 minutes). We demonstrate the utility of ^{35}Cl SSNMR for providing distinct fingerprints for each urea MCC and detecting chlorine-containing impurities. Dispersion-corrected plane-wave DFT-D2* calculations are used for structural refinement and relating ^{35}Cl electric field gradient (EFG) tensors and chloride ion hydrogen bonding environments. Finally, ab $initio$ molecular dynamics calculations are used to study the impact of molecular motions on ^{35}Cl EFG tensors, and their concomitant use for site assignment and NMR crystallography. Together, these techniques show great promise for future development of crystal structure prediction protocols using NMR of quadrupolar nuclei.

1. Introduction

The rational design of single-phase multi-component crystals (MCCs) is a flourishing area in the fields of crystal engineering and pharmaceutical sciences.[1,2] Solid forms of MCCs include solvates, salts, cocrystals, and combinations thereof; these are of particular interest to the pharmaceutical industry, as they can be made from an active pharmaceutical ingredient (API) and one or more pharmaceutically-acceptable coformers (*i.e.*, pharmaceutical cocrystals, PCCs).[3,4] By carefully selecting the appropriate constituents and mode(s) of preparation, it is possible to tailor the physicochemical properties (*i.e.*, solubility, stability, and/or bioavailability) of MCCs for specific applications.[5–8]

Mechanochemical synthesis (*i.e.*, synthetic techniques that induce chemical changes with mechanical action) offers unique opportunities for the production of MCCs.[9–11] One common mechanochemical synthetic methods is ball milling, where solid reagents are ground at a constant milling frequency using ball bearings in a sealed jar. Mechanochemical syntheses offers many advantages over crystallization from solution, including rapid production of solid-phase products in minutes (as opposed to days by crystallization), high yields, and potential production of novel solid forms that are either difficult or impossible to obtain by crystallization.[9,10,12–16] Furthermore, mechanochemical synthesis adheres to many of the tenets of *green chemistry*, including minimal use of solvent, low energy input, atom economy, and reduction of waste and/or by-products.[10,13,16–18]

There are several techniques for characterizing products of mechanochemical syntheses, including X-ray diffraction (XRD), calorimetric analysis (*i.e.*, thermogravimetric analysis and differential scanning calorimetry), vapour sorption analysis, vibrational spectroscopy (*i.e.*, infrared and Raman spectroscopies), and

[a] Department of Chemistry & Biochemistry, Florida State University, Tallahassee, FL 32306, USA. E-mail: rschurko@fsu.edu
[b] National High Magnetic Field Laboratory, Tallahassee, FL 32310, USA
[c] Department of Chemistry & Biochemistry, University of Windsor, Windsor, ON, N9B 3P4, USA
† Electronic supplementary information (ESI) available. See DOI: 10.1039/d1ce01610e

solid-state NMR (SSNMR) spectroscopy.[19] Single-crystal X-ray diffraction (SCXRD) generally has limited applicability for characterizing the products of mechanochemical syntheses, which tend to be microcrystalline powders (hence, powder XRD, PXRD, is more often used). Of these methods, SSNMR spectroscopy provides the most detailed information about molecular-level structure and dynamics for materials ranging in nature from highly crystalline to completely amorphous. Moreover, SSNMR is increasingly being used in the context of NMR crystallography,[20–27] an important set of techniques that holds much promise for improving crystal structure prediction (CSP) methods.[28–31]

NMR crystallography utilizes SSNMR spectroscopy, XRD methods, and quantum chemical calculations to solve, refine, and/or validate crystal structures.[20–27] Density functional theory (DFT) calculations of chemical shifts (*i.e.*, most commonly ^{1}H, ^{13}C, and ^{15}N) aid in structural refinements and can be used as a figure of merit for assessing the quality of structures of organic solids.[32–41] However, there are many classes of organic solids with cationic or anionic species that have quadrupolar NMR-active nuclides (*i.e.*, nuclear spin $I > \frac{1}{2}$; *e.g.*, ^{7}Li, ^{23}Na, $^{35/37}$Cl, ^{39}K, $^{79/81}$Br, *etc.*). Acquisition of the SSNMR spectra of such nuclides permits the determination of their electric field gradient (EFG) tensors, which are extremely sensitive to even the most subtle structural changes or differences, as well as to longer-range interactions, providing a unique source of additional structural information.[42–50] In turn, comparison of experimentally measured and computationally derived EFG tensors offers an alternative means of refining crystal structures (and possibly even identifying potential structures in conjunction with CSP methods) that do not depend solely on the measurement, assignment, and computation of chemical shifts. Moreover, quantum chemical calculations of EFG tensors are much less computationally expensive than those of chemical shifts, since the former depend only on the electronic ground state of the molecule. Furthermore, in certain situations, the calculation of both EFG and CS tensors can be a very powerful means of structural refinement, since their corresponding interactions have independent physical origins. As such, it is desirable to develop NMR crystallographic techniques that use quadrupolar parameters for crystal structure prediction, refinement, and validation.[46,51–62]

Of the commonly occurring quadrupolar nuclei in organic solids, ^{35}Cl ($I = 3/2$) is the most widely explored from the perspective of structural refinements based on the measurement and computation of EFG tensors;[45,47,56,59,63–69] this is due to both the preponderance of hydrochloride (HCl) salts of organic solids (such as APIs) and the relative ease of measurement of ^{35}Cl SSNMR spectra of chloride ions. ^{35}Cl SSNMR spectra feature central transition (CT, $+\frac{1}{2} \leftrightarrow -\frac{1}{2}$) powder patterns that are influenced by the second-order quadrupolar interaction (SOQI) and chemical shift anisotropy (CSA). The magnitudes of the principal components of the ^{35}Cl EFG tensor, as well as its orientation with respect to the molecular frame, are sensitive to the local electronic environment of the chloride ion. Slight differences in the hydrogen bonding environments of chloride

ions have dramatic impacts on their ^{35}Cl EFG tensors, resulting in distinct sets of quadrupolar parameters (*i.e.*, the quadrupolar coupling constant, C_Q, and the asymmetry parameter, η_Q) for even very small differences or changes in structure; as such, ^{35}Cl SSNMR spectra often yield unique spectral fingerprints, making them useful for the differentiation of polymorphs, hydrates, solvates, and other solid forms of organic HCl salts, as well as the detection of impurity phases.[42,45,47,56,59,63–68]

In order to design an NMR crystallography protocol that can be used for solving crystal structures of MCCs involving cationic and/or ionic species, including PCCs, a series of simple candidate systems is required that meet the following criteria: (i) elementary chemical structures; (ii) small numbers of atoms in the asymmetric units; and (iii) abundance of useful NMR handles. One family of MCCs that meets these criteria is urea MCCs (*i.e.*, MCCs comprised of urea molecules and other elementary ionic species). Urea remains a vital reagent in many areas of chemistry,[70–76] and is able to form supramolecular assemblies such as inclusion compounds[77–80] and cocrystals,[72,73,81–84] which can be synthesized mechanochemically in some cases. Urea is an ideal molecule for investigation of the syntheses and structures of MCCs, as well as for benchmarking NMR crystallographic protocols, since it is small and has both hydrogen-bond donor and acceptor groups.

Herein, we discuss the mechanochemical preparation of urea MCCs and their structural characterization using ^{35}Cl and ^{13}C SSNMR spectroscopy, PXRD and/or SCXRD, and DFT calculations. Novel ball milling preparations of the MCCs NEt$_4$Cl:2Urea, NEt$_4$Cl:2Urea·2H$_2$O, NPr$_4$Cl:2Urea, NPr$_4$Cl:3Urea, and NH$_4$Cl:Urea, which are aimed at maximizing yield and optimizing efficiency, are described, and contrasted with previously-reported preparations featuring crystallization from solution. The identities and purities of the products of mechanochemical syntheses (*i.e.*, MCCs, starting educts, and other potential impurities) are confirmed using ^{35}Cl SSNMR and PXRD. Dispersion-corrected plane-wave DFT-D2* calculations[58,85] are used to refine the crystal structures, assess the agreement between experimentally measured and theoretically derived ^{35}Cl EFG tensors, and elucidate relationships between NMR parameters and molecular-level structure. *Ab initio* molecular dynamics (*ai*MD) simulations are used to probe the impact of molecular motions upon ^{35}Cl EFG tensors, and to gauge the possibility of using such calculations for site assignments and NMR crystallographic analyses. Finally, we discuss the potential of these characterization methods for use in the design of NMR crystallographic-based CSP protocols for determining the structures of complex MCCs and PCCs.

2. Experimental and computational methods

2.1 Materials and syntheses

Ammonium chloride (NH$_4$Cl), tetraethylammonium chloride monohydrate (NEt$_4$Cl·H$_2$O), tetra(*n*-propyl)ammonium

chloride (NPr$_4$Cl), urea, and solvents were purchased from Sigma Aldrich Canada Ltd. The solid educts were oven-dried prior to use at 110 °C for 16 hours, and their identities and purities verified using PXRD (Fig. S1†).

Each MCC was prepared mechanochemically *via* ball milling of the dried reagents (and microliter quantities of H$_2$O where indicated) in the appropriate molar ratios (Table S1†). These syntheses used a Retsch Mixer Mill 400, 10 mL stainless steel milling jars, and two 7 mm stainless steel ball bearings. The total mass of the solid reagents in each synthesis was scaled to *ca.* 200 mg. The maximum milling rate of 30 Hz was used for all syntheses. All syntheses were optimized to obtain maximum yield and optimized efficiency.

Crystals of NH$_4$Cl:Urea, suitable for analysis by SCXRD, were grown by slow evaporation of an aqueous solution of equimolar NH$_4$Cl and urea. Crystals of NPr$_4$Cl were grown from a saturated DCM solution *via* slow diffusion of anhydrous pentane.

2.2 Powder X-ray diffraction

For all materials except NPr$_4$Cl, PXRD patterns were acquired using a Rigaku MiniFlex benchtop diffractometer with a Cu K$_\alpha$ (λ = 1.541 Å) radiation source and a D/teX Ultra2 detector. Samples were packed in zero-background silicon wafers with a well size of 5 mm × 0.2 mm, and mounted on an eight-position autosampler. Experiments were conducted with an X-ray tube voltage of 40 kV, an amperage of 15 mA, 2θ angles ranging from 5–50°, a step size of 0.030°, and a dwell time of 5 s, resulting in an acquisition time of *ca.* 12 minutes per sample.

For NPr$_4$Cl, the PXRD pattern was acquired using a Rigaku Smartlab diffractometer with a Cu K$_\alpha$ radiation source and a D/teX Ultra2 detector. The sample was packed on a zero-background wafer and mounted in an air-tight sample holder. Experiments were conducted with an X-ray tube voltage 40 kV, an amperage of 44 mA, a length limiting slit of 5 mm, 2θ angles ranging from 5–50°, a step size of 0.030°, and a dwell time of 5 s, resulting in an acquisition time of *ca.* 12 minutes per sample.

The CrystalDiffract software package was used to simulate PXRD patterns for materials with known crystal structures.

2.3 Single-crystal X-ray diffraction

Crystals of NH$_4$Cl:Urea or NPr$_4$Cl were mounted on a cryoloop using paratone oil. Data were collected using φ and ω scans at a temperature of either 170(2) K or 150(2) K on a Bruker D8 Venture four-circle diffractometer equipped with a Photon 100 CCD detector using Mo K$_\alpha$ radiation (λ = 0.7107 Å). The temperature was controlled using an Oxford Cryosystems Cryostat (700 Series Cryostream Plus). An appropriate data collection strategy was determined using APEX III software,[86] based on an initial cell indexing. The raw data were integrated and reduced using SAINT,[86] and corrected for absorption effects using SADABS.[86] Structures were solved using intrinsic phasing[87] and refined against F^2

with SHELXL[88] within OLEX2.[89] The positions of all non-hydrogen atoms were refined anisotropically. Hydrogen atoms were placed in idealized positions and refined using a riding model for NPr$_4$Cl, or by Fourier difference maps and refined isotropically for NH$_4$Cl:Urea. The structures of NPr$_4$Cl and NH$_4$Cl:Urea have been deposited on the Cambridge Structural Database [CSD deposition numbers 2120237 and 2120238, respectively].

2.4 Solid-state NMR spectroscopy

Overview. All NMR data corresponding to a field strength of 9.4 T were obtained at the University of Windsor (Windsor, Ontario, Canada) using a Bruker Avance III HD spectrometer and an Oxford wide-bore magnet, with Larmor frequencies of $\nu_0(^1H)$ = 400.24 MHz and $\nu_0(^{35}Cl)$ = 39.21 MHz. Static experiments were conducted using a Revolution 5 mm HX static probe, with samples packed in 5 mm o.d. glass tubes, whereas spinning experiments were conducted using a Varian/Chemagnetics 4 mm HXY magic angle spinning (MAS) probe, with samples packed in 4 mm o.d. zirconia rotors. All data corresponding to a field strength of 14.1 T were obtained at the National High Magnetic Field Laboratory (Tallahassee, FL) using a Bruker NEO console and an Oxford wide-bore magnet, with Larmor frequencies of $\nu_0(^1H)$ = 600.07 MHz, $\nu_0(^{13}C)$ = 150.87 MHz, and $\nu_0(^{35}Cl)$ = 58.79 MHz. These experiments used a home-built 3.2 mm HXY MAS probe with samples packed into 3.2 mm o.d. zirconia rotors. All data corresponding to a field strength of 19.5 T were obtained at the National High Magnetic Field Laboratory using a Bruker NEO console and an Oxford 31 mm bore magnet, with Larmor frequencies of $\nu_0(^1H)$ = 831.48 MHz and $\nu_0(^{35}Cl)$ = 81.47 MHz. These experiments used a home-built 3.2 mm HX MAS probe with samples packed into 3.2 mm o. d. zirconia rotors. A summary of all experimental parameters is found in the ESI.†

^{35}Cl{^{1}H} **SSNMR.** All ^{35}Cl spectra were acquired under static or MAS (ν_{rot} = 5–16 kHz) conditions using a Hahn-echo pulse sequence with CT-selective $\pi/2$ pulses, with the exception of the MAS spectrum of NPr$_4$Cl, which was acquired using non-selective $\pi/2$ pulses. ^{1}H continuous-wave decoupling was used in all experiments, with a decoupling field of either 25 kHz (9.4 T) or 55 kHz (19.5 T). All ^{35}Cl SSNMR spectra presented in this work were acquired with calibrated recycle delays to ensure maximum signal to noise and to allow for quantification of relative numbers of chloride ion sites (in the cases of multiple sites in the products and/or sites arising from impurities or leftover educts). The ^{35}Cl chemical shifts were referenced to solid NaCl (δ_{iso} = 0.0 ppm), sometimes employing 0.1 M NaCl (aq) (δ_{iso} = −41.11 ppm) as a secondary chemical shift reference.[90] Spectra were processed using TopSpin 4.1[91] and simulations of all ^{35}Cl powder patterns were prepared using ssNake v1.3,[92] which uses the *ZX′Z″* convention for the Euler angles. The Euler angles were converted to the *ZY′Z″* convention[93–95] for direct comparison to the relative tensor

orientations extracted from CASTEP calculations using the EFGShield software package,[95] which uses the *ZY'Z"* convention (see ESI† S1 for details). Uncertainties were assessed through bidirectional variation of each parameter, and visual comparison of experimental and simulated spectra.

$^1H\rightarrow ^{13}C\{^1H\}$ CP/MAS SSNMR. A ramped amplitude $^1H\rightarrow ^{13}C$ cross-polarization (CP)/MAS pulse sequence[96,97] was used to acquire the ^{13}C SSNMR spectra, with spinning rate of v_{rot} = 6 kHz. A SPINAL-64 ^1H decoupling field of $v_2(^1H)$ = 100 kHz and a 2 ms contact time with a Hartman–Hahn matching field of $v_1(^1H)$ = 50 kHz were used in all experiments. Chemical shifts were referenced to TMS ($\delta_{iso}(^{13}C)$ = 0.0 ppm) *via* the secondary methylene resonance of adamantane at $\delta_{iso}(^{13}C)$ = 38.57 ppm.[98]

2.5 Density functional theory calculations

Overview. All calculations were performed using plane-wave DFT as implemented in the CASTEP module of BIOVIA Materials Studio 2020,[99] using model structures obtained from XRD studies. These calculations employed the RPBE functional[100] and ZORA/scalar ultrasoft pseudopotentials generated on the fly.[101] All calculations employed a version of the Grimme two-body dispersion correction[102] that has been reparameterized to aid in the refinement of the crystal structures of organic solids and the calculation of EFG tensors.[57,58,85]

Geometry optimizations. Structural refinements of the atomic positions within the crystal structures employed the low-memory BFGS energy-minimizing scheme.[103] Only the atomic positions were allowed to vary, while holding the unit cell parameters from the reported crystal structures at 170 K constant. The reason for this is that semi-empirical, two-body force fields, such that of Grimme, are known to overestimate unit cell volumes due to their approximate nature – this places strict limitations on allowing free geometry optimization of the unit cell.[58,104] Calculations used an SCF convergence threshold of 5×10^{-7} eV atom^{-1}, plane-wave cutoff energy of 800 eV, and evaluated integrals over the Brillouin zone using a Monkhorst-Pack grid with a k-point spacing of 0.05 Å^{-1}.[105] The thresholds for structural convergence were a maximum change in energy of 5×10^{-6} eV atom^{-1}, and a maximum displacement of 5×10^{-4} Å atom^{-1}.

Ab initio molecular dynamics. *ai*MD simulations on structural models of NH$_4$Cl:Urea were performed within the extended-Lagrangian Born–Oppenheimer molecular dynamics (xL–BOMD) formalism.[106–108] The model system was treated as a canonical *NVT* ensemble. The randomized initial ionic velocities were stabilized at equilibrium values by employing a 300 K Nosé–Hoover–Langevin thermostat.[109] A time step of 0.5 fs was used with a total simulation time of 10.5 ps (*i.e.*, 21 000 total steps). The unit cell was altered from *Pmna* symmetry to a supercell with $P_{\bar{1}}$ symmetry, which increases the number of unique chlorine environments from two to

eight. These calculations employed an SCF threshold of 2×10^{-6} eV atom^{-1}, a plane-wave cutoff energy of 325 eV, and evaluated integrals over the Brillouin zone using a Monkhorst-Pack grid with a k-point spacing of 0.10 Å^{-1}.

NMR interaction tensors. ^{35}Cl EFG tensors and magnetic shielding tensors were calculated using the same SCF threshold, plane-wave cutoff energy, and k-point spacing as the geometry optimizations. ^{35}Cl magnetic shielding tensors were calculated using the GIPAW approach,[110] and magnetic shielding values were converted to the chemical shift scale by setting the calculated shielding of NH$_4$Cl to δ_{iso} = 120 ppm relative to that of solid NaCl at δ_{iso} = 0 ppm. For the time-averaged calculations of NMR interactions, a total of 100 snapshot structures were selected using direct Monte Carlo sampling of structures along the MD trajectory (excluding data from the first 1000 time steps (0.5 ps)). Since there are four unique crystallographic chlorine sites in the supercells, this led to the sampling of 400 snapshots of the molecular-level local environments of the chloride ions.

3. Results and discussion

Here, we discuss (i) the characterization of the reagents NH$_4$-Cl, NPr$_4$Cl, and NEt$_4$Cl·H$_2$O by $^{35}Cl\{^1H\}$ SSNMR spectroscopy, (ii) the synthesis and characterization of urea MCCs involving either NEt$_4$Cl or NPr$_4$Cl, as well as a comparison of their experimental and calculated ^{35}Cl EFG tensors, and (iii) the synthesis and characterization of NH$_4$Cl:Urea, which is distinct from all of the other systems, due to molecular-level motions that influence the measurement of ^{35}Cl EFG tensors. PXRD and ^{13}C SSNMR spectroscopy are used as supporting characterization techniques (Fig. S2 and S3, and Table S2†). We also report a novel crystal structure of NPr$_4$Cl at 150 K and redetermine the crystal structure of NH$_4$Cl:Urea at 170 K (Fig. S4 and Table S3†).

In all cases, ^{35}Cl SSNMR spectra were acquired at two distinct magnetic fields to aid in the precise determination of the principal components of the EFG and CS tensors, since the manifestations of the SOQI and CSA in CT powder patterns have distinct dependences on the strength of the magnetic field (*i.e.*, the effects of the former and latter scale proportionally to B_0^{-1} and B_0, respectively, for most sets of Euler angles describing the relative orientation of the EFG and CS tensors, *vide infra*).[95] Additionally, acquisition of ^{35}Cl MAS NMR spectra allows for accurate determination of the δ_{iso}, C_Q, and η_Q, due to the averaging of the ^{35}Cl CSA (under a high enough MAS rate) and partial averaging of the SOQI; this aids in the fitting of the static NMR spectra using eight parameters, including the span (Ω), and skew (κ) of the CS tensor, and the aforementioned Euler angles (α, β, and γ) (see Table 1 for definitions of all parameters).

The values of the quadrupolar parameters determined from analysis of ^{35}Cl CT patterns are of great value, since they are directly related to the principal components of the EFG tensor, which in turn provides information on the local ground state electron density about the chloride ions.[111–113]

Table 1 Summary of experimental and calculated ^{35}Cl EFG and CS tensor parameters^{a,b,c,d,e}

Material (Cl site)		C_Q (MHz)	η_Q	δ_{iso} (ppm)	Ω (ppm)	κ	α (°)	β (°)	γ (°)
NEt$_4$Cl:2Urea	Exp.	1.82(9)	0.95(5)	93(1)	54(4)	0.05(3)	4(10)	30(3)	110(5)
	DFT-D2*	−1.71	0.87	85	88	−0.14	4	42	99
	XRD^e	2.35	0.67	62	72	−0.05	151	33	303
NEt$_4$Cl:Urea·2H$_2$O	Exp.	2.88(4)	0.95(2)	61(2)	78(10)	0.51(8)	82(6)	3(5)	173(9)
	DFT-D2*	−3.27	0.88	53	73	0.57	76	2	36
	XRD^f	—	—	—	—	—	—	—	—
NPr$_4$Cl:2Urea	Exp.	2.73(3)	0.79(4)	79(1)	81(3)	0.80(6)	83(10)	75(10)	132(20)
	DFT-D2*	2.84	0.69	70	84	0.57	90	78	162
	XRD	2.75	0.47	48	74	0.6	90	70	190
NPr$_4$Cl:3Urea	Exp.	0.92(1)	0.76(2)	91(1)	57(7)	0.53(6)	36(5)	66(4)	90(5)
	DFT-D2*	−1.32	0.89	83	42	0.19	202	58	216
	XRD	2.10	0.25	57	36	0.34	179	34	200
NH$_4$Cl:Urea (Cl1)	Exp.	3.52(5)	0.14(7)	103(2)	98(7)	0.00(8)	90(5)	77(7)	178(4)
	DFT-D2*	−3.33	0.53	102	98	−0.49	90	1	180
	XRD	3.39	0.74	71	88	0.13	90	58	180
NH$_4$Cl:Urea (Cl2)	Exp.	2.62(6)	0.49(5)	100(2)	71(5)	0.78(10)	89(25)	8(5)	178(30)
	DFT-D2*	4.63	0.34	91	92	0.24	90	76	90
	XRD	−2.50	0.90	74	86	−0.44	90	11	90
NH$_4$Cl	Exp.	< 0.03	n/a	120(1)	n/a	n/a^g	n/a	n/a	n/a
	DFT-D2*	0	n/a	120	0	n/a	n/a	n/a	n/a
	XRD^f	—	—	—	—	—	—	—	—
NPr$_4$Cl	Exp.	0.16(2)	0^d	57(1)	14(2)	−1.00^d	90^d	90^d	180^d
	DFT-D2*	0.1	0	58	17	−1.00	90	90	180
	XRD	−0.05	0	44	17	−1.00	90	90	180

The experimental uncertainties in the last digit for each value are indicated in parentheses. ^{a} The principal components of the EFG tensors are ranked $|V_{33}| \geq |V_{22}| \geq |V_{11}|$. The quadrupolar coupling constant and asymmetry parameter are given by $C_Q = eQV_{33}/h$, and $\eta_Q = (V_{11} − V_{22})/V_{33}$, respectively. The sign of C_Q cannot be determined from the experimental ^{35}Cl spectra. ^{b} The principal components of the chemical shift tensors are defined using the frequency-ordered convention such that $\delta_{11} \geq \delta_{22} \geq \delta_{33}$. The isotropic chemical shift, span, and skew are given by $\delta_{iso} = (\delta_{11} + \delta_{22} + \delta_{33})/3$, $\Omega = \delta_{11} − \delta_{33}$, and $\kappa = 3(\delta_{22} − \delta_{iso})/\Omega$, respectively. ^{c} The Euler angles α, β, and γ define the relative orientation of the EFG and chemical shift tensors. Euler angles are reported using the $ZY'Z''$ convention. ^{d} The fits for these patterns were constrained using parameters obtained from DFT calculations. ^{e} Theoretical EFG and CS tensor parameters were obtained from calculations on XRD-derived structures and structures refined at the RPBE-D2* level. ^{f} The positions of hydrogen atoms were not reported in these crystal structures. ^{g} This parameter is not applicable or has little-to-no effect on the simulated ^{35}Cl SSNMR pattern.
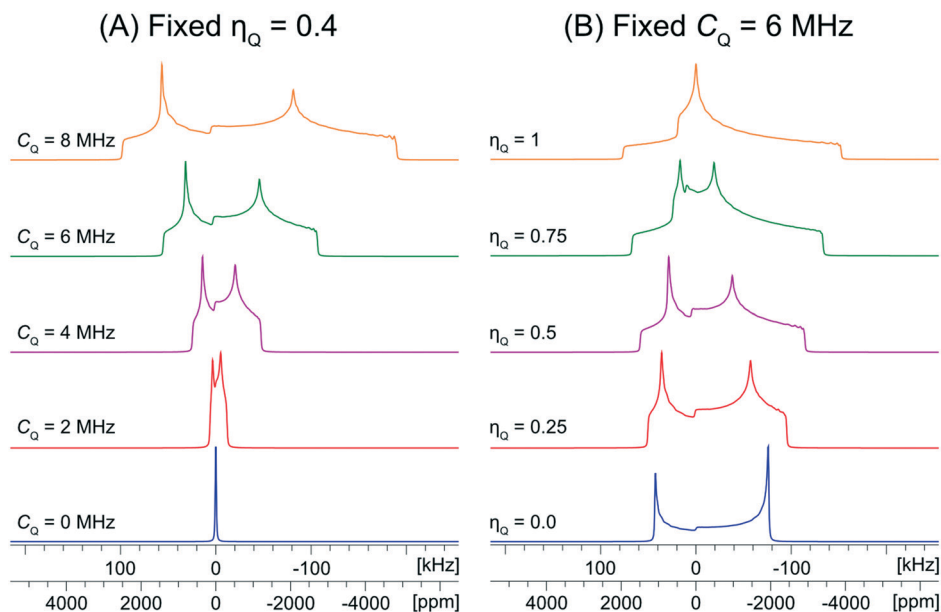
Scheme 1 Analytical simulations of ^{35}Cl central transition NMR spectra under static conditions at B_0 = 9.4 T. (A) Shows values of C_Q ranging from 0 to 8 MHz with a fixed η_Q = 0.4 and (B) shows values of η_Q ranging from 0 to 1 with a fixed C_Q = 6 MHz. The range of C_Q values is selected to be representative of those typically observed for chloride ions.

Increased values of C_Q, which result in broadening of the CT patterns (Scheme 1A), correspond to ground state electron distributions that increasingly depart from spherical (platonic) symmetry. For instance, if the electronic environment of a chloride ion is perturbed by hydrogen bonding, the absolute magnitude of C_Q is generally observed to increase. On the other hand, values of η_Q, which produce patterns where the discontinuities adopt different relative positions (Scheme 1B), describe the axial symmetry of the EFG tensor, and correspondingly, the cylindrical symmetry of the ground state electron density ($0 \leq \eta_Q \leq 1$, where $\eta_Q = 0$ indicates perfect axial symmetry). For example, a Cl atom involved in a covalent C–Cl bond typically has an axially symmetric EFG tensor ($\eta_Q = 0$), whereas Cl$^-$ ions featuring multiple short H⋯Cl hydrogen bonds often have non-axially symmetric EFG tensors ($\eta_Q \neq 0$). Unfortunately, interpretation of chlorine CS tensors is not as straightforward as this and relies heavily upon computationally expensive DFT calculations; hence, we will focus on exploring relationships between structure, symmetry, and ^{35}Cl EFG tensors throughout this work.

3.1 Educts: NH$_4$Cl, NPr$_4$Cl, and NEt$_4$Cl·H$_2$O

The characterization of the educts is important, primarily for the purpose of identifying their potential presence in the reaction products arising from either ball milling or recrystallization from solution. Fortunately, each of the ammonium chloride salts yields a distinct ^{35}Cl NMR spectral fingerprint (Fig. 1).

The static and MAS ^{35}Cl{^{1}H} SSNMR spectra (9.4 T) of NH$_4$Cl are narrow and nearly featureless, indicating a single chlorine environment with negligible influence from the SOQI ($C_Q < 30$ kHz) or CSA; this observation is consistent with the cubic space group of its crystal structure ($Pm\bar{3}m$, $Z' = 1$, $Z = 1$), in which the chloride ion sits at a site of local octahedral symmetry.[114]

The ^{35}Cl{^{1}H} MAS spectrum (9.4 T) of NPr$_4$Cl is characterized by a sharp, featureless centerband corresponding to the CT, and a manifold of spinning sidebands (SSBs) arising from the satellite transitions (STs, $\pm 3/2 \leftrightarrow \pm 1/2$). Fitting this spectrum yields $\delta_{iso} = 57(1)$ ppm, $C_Q = 160(20)$ kHz, and $\eta_Q = 0.0$. The ^{35}Cl static CT spectrum of NPr$_4$Cl is dominated by the effects of CSA and characterized by $\Omega = 14(2)$ ppm and $\kappa = -1.0$. The CSA is small and has no observable influence on the SSBs in the MAS spectrum. The crystal structure of NPr$_4$Cl is in the tetragonal space group $I\bar{4}$ ($Z' = 0.25$, $Z = 2$), with a single chlorine environment in the asymmetric unit. The magnitude of C_Q is very small because the chloride ion, which is positioned on the C_4 axis of the tetragonal unit cell, does not participate in hydrogen bonding with the surrounding NPr$_4$$^+$ ions (i.e., all H⋯Cl$^-$ distances are greater than 2.8 Å).[115]

Finally, the ^{35}Cl{^{1}H} NMR spectra of NEt$_4$Cl·H$_2$O feature patterns that are substantially broader and more complex than those of the other educts, clearly indicating the effects of the SOQI. The NMR spectra are simulated with a minimum of three overlapping patterns, based upon the number of visible discontinuities in the MAS spectra, with values of C_Q that are larger than those observed for NH$_4$Cl and NPr$_4$Cl (Table S4†). These broader patterns are clearly indicative of H⋯Cl$^-$ hydrogen bonds between the chloride ions and surrounding water molecules. The ratios of the integrated intensities for the three overlapping patterns are ca. 2:4:1 (MAS) and 1:4.4:1.4 (static). Assuming the presence of only three patterns with distinct quadrupolar parameters, these spectra indicate the presence of three magnetically non-equivalent chloride ion sites. At first, this
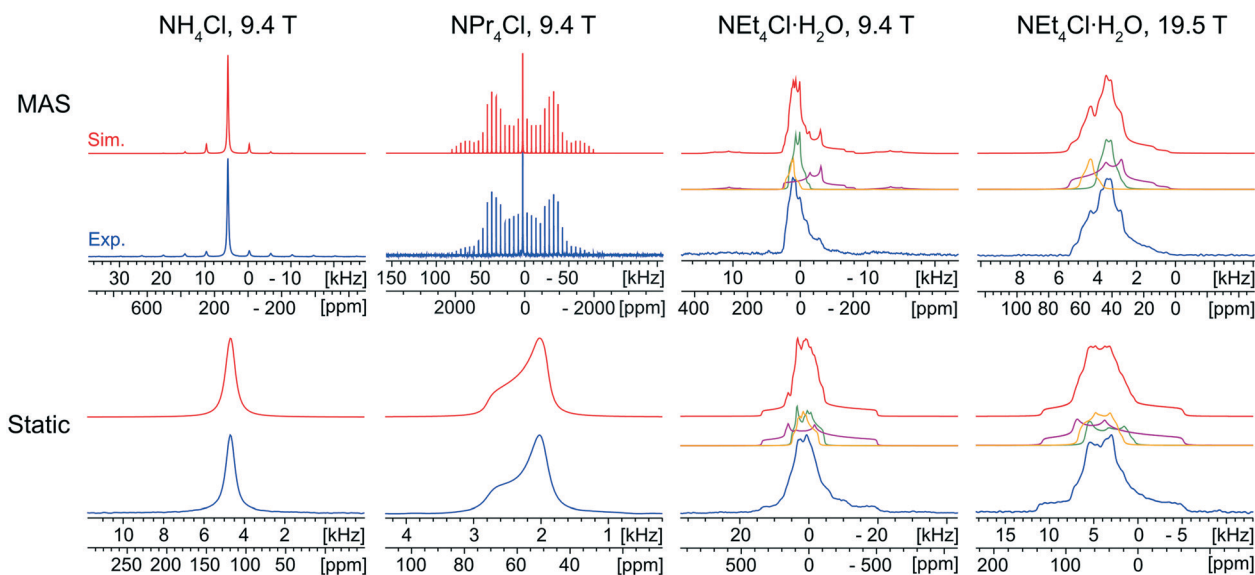

Fig. 1 Experimental ^{35}Cl{^{1}H} SSNMR spectra (lower traces) of NH$_4$Cl, NPr$_4$Cl, and NEt$_4$Cl·H$_2$O acquired at 9.4 T and 19.5 T under MAS (v_{rot} = 5–16 kHz, top) and static (bottom) conditions, with corresponding analytical simulations (upper traces) and deconvolutions (middle traces). The spectra of NEt$_4$Cl·H$_2$O were fit with three overlapping patterns with a 2:4:1 ratio of integrated intensities (green:purple:yellow).

would seem to be inconsistent with the known crystal structure ($C2/c$, $Z' = 1$, $Z = 8$), which comprises a single crystallographically distinct chloride ion. The presence of multiple patterns could arise from local disorder in the ethyl moieties (which is predicted in the crystal structure, and verified by the presence of eight distinct methyl peaks in the $^1H \rightarrow ^{13}C\{^1H\}$ CP/MAS spectrum, Fig. S2A†).[116] This system could be a subject for future investigations, but is beyond the scope of the current work – for now, the ^{35}Cl CT patterns of NEt$_4$Cl·H$_2$O are strictly used to identify the presence of educt, if present.

3.2 NR$_4$Cl:xUrea·yH$_2$O (R = Et, Pr; x = 1, 2, 3; y = 0, 2)

Mechanochemical syntheses of NEt$_4$Cl:2Urea, NEt$_4$Cl:Urea·2H$_2$O, NPr$_4$Cl:2Urea, and NPr$_4$Cl:3Urea were all successful, as judged by comparison of PXRD patterns of the solid products with simulated PXRD patterns based on the known crystal structures (Fig. S5, Table S5†).[117–119] It is noteworthy, however, that this does not preclude the presence of impurity phases, rather that the quantity of impurity phase(s) is low, typically <5–10%, *vide infra*.[120] Initial trials revealed that all MCCs could be

mechanochemically synthesized in 30–40 minutes, which is a significant improvement over growing single crystals *via* crystallization from solution, which can require several days.[75] Remarkably, further optimizations revealed that most MCCs could be prepared much more quickly, with NEt$_4$-Cl:2Urea, NPr$_4$Cl:2Urea, and NPr$_4$Cl:3Urea taking only one minute (there was no reduction in preparation time for NEt$_4$-Cl:Urea·2H$_2$O, which took 40 minutes, Table S1, Fig. S6–S10†). Some mechanochemical syntheses attempted with shorter milling times resulted in impurities that are detectable *via* PXRD (Fig. S6–S10†). Interestingly, the anhydrous NEt$_4$Cl:2Urea and hydrated NEt$_4$Cl:Urea·2H$_2$O MCC products are dependent upon the ratio of urea to NEt$_4$-Cl·H$_2$O educts (*i.e.*, 1:2 and 1:1, respectively). Preparations of NEt$_4$Cl:Urea·2H$_2$O with 0, 1, and 2 eq. of H$_2$O yields products with similar pXRD patterns (Fig. S11†), indicating that in the case of the mechanochemical reaction with no additional liquid, water must come from the educt hydrate and the atmosphere.

The ^{35}Cl SSNMR spectra of these MCCs acquired under static and MAS conditions at 9.4 T and 19.5 T (Fig. 2) are distinct from those of the simple ammonium chloride salts (*cf.* Fig. 1), indicating that no impurity phases are present (*N.*
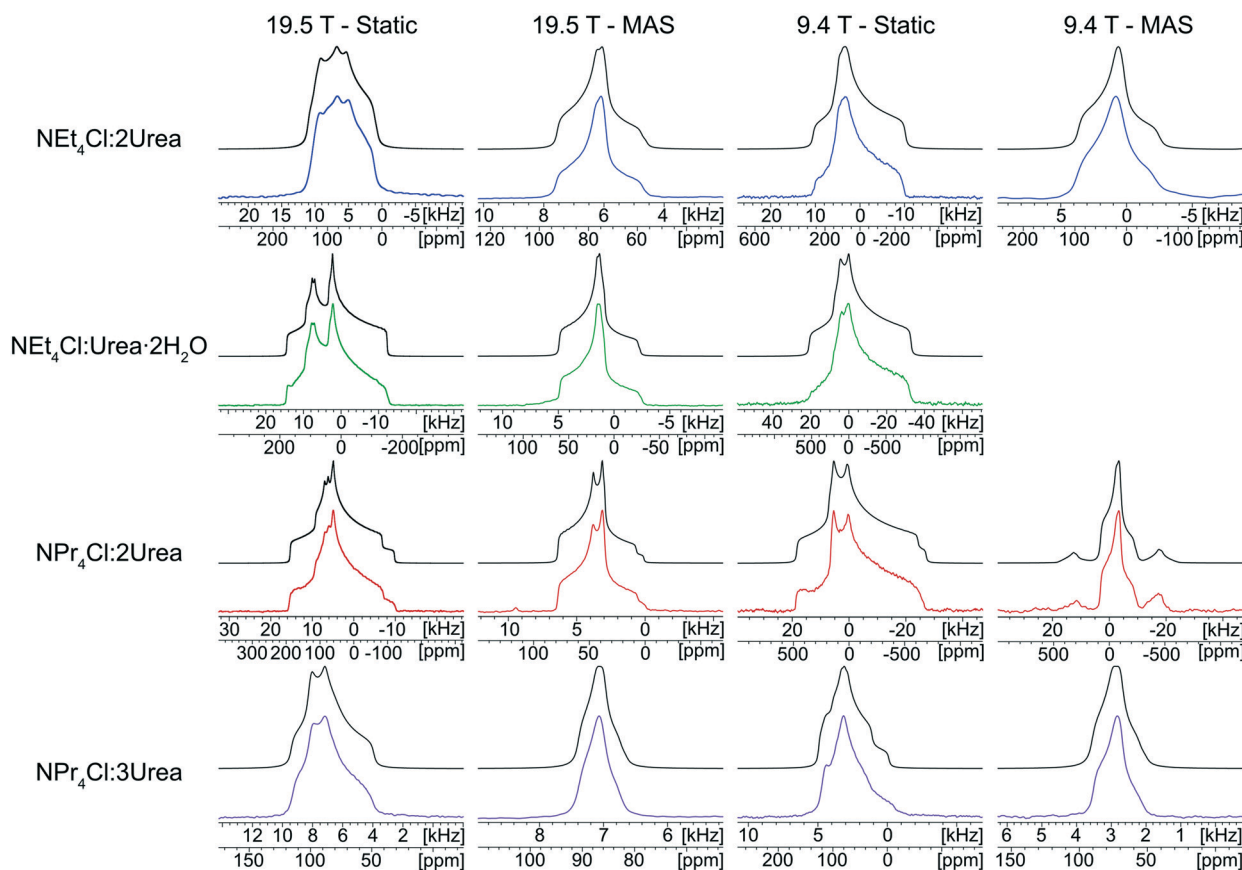

Fig. 2 Experimental $^{35}Cl\{^1H\}$ SSNMR spectra of tetraethyl- and tetra(n-propyl)ammonium chloride:Urea MCCs (lower traces) and corresponding analytical simulations (upper traces). Data were acquired at two fields (B_0 = 9.4 T and 19.5 T) under static and MAS conditions (ν_{rot} = 10–15 kHz). A MAS spectrum of NEt$_4$Cl:Urea·2H$_2$O was not acquired at 9.4 T since we were unable to spin fast enough to fully separate the spinning sidebands from the isotropic centerband.

B.: in many instances, carefully designed SSNMR experiments can quantitatively detect small amounts of impurities that are not always evident in PXRD patterns).[38,64,121–124] In each spectrum, a CT pattern dominated by the SOQI is observed that corresponds to a single magnetically and crystallographically distinct chloride ion, in accordance with the reported crystal structures, where all four MCCs are reported to crystallize in either the monoclinic $P2_1/c$ or $P2_1/n$ space groups (Table S5†) and have one crystallographically distinct chloride ion in the asymmetric unit ($Z' = 1$, $Z = 4$).[117–119] The ^{35}Cl EFG tensor parameters obtained from the analytical simulations feature values of C_Q between 0.96(1) MHz and 2.88(4) MHz (Table 1), which are within the typical range observed for organic HCl salts.[90] Additionally, the value of the asymmetry parameter is found to be high ($\eta_Q \geq 0.70$) in each case.

Relationships between the NMR parameters and crystal structures can be elucidated with quantum chemical calculations. Recent studies have demonstrated the use of plane-wave DFT calculations with semiempirical dispersion-corrected force-fields that result in higher quality crystal structures and more accurate predictions of EFG tensors than is possible from DFT calculations not employing these methods.[41,57,58,85] This force-field correction, DFT-D2*, based on a modification on Grimme's two-body model,[102] was developed through refinements of the crystal structures of various organic solids and subsequent calculations of ^{35}Cl, ^{14}N, and ^{17}O EFG tensors.[41,57,58,85] Structural models based on the reported crystal structures for each MCC were subjected to geometry optimizations using the DFT-D2* method. The ^{35}Cl EFG tensors were calculated for both XRD-derived and DFT-D2* structural models and compared with experimentally determined tensors (Fig. 3). The RMS EFG distance[58] is used as a figure of merit for assessing the agreement between calculated and experimental ^{35}Cl EFG tensors. The DFT-D2* calculations result in better agreement between calculation and experiment, since the RMS EFG distance is $\Gamma_{RMS} = 0.53$ MHz for the XRD-derived models, and much lower, $\Gamma_{RMS} = 0.21$ MHz, for the DFT-D2* models (ESI† S2), which is consistent with our previous work.[58,63] The structural models with atomic coordinates refined at the

DFT-D2* level indicate that each chloride ion features between four and six H⋯Cl$^-$ contacts with urea and/or water molecules (Table 2) that are all greater than *ca.* 2.2 Å, which is consistent with the small magnitudes of C_Q.[45]

The orientations of the principal components of the ^{35}Cl EFG tensors in their molecular frames give insight into the local chloride ion hydrogen-bonding environments (Fig. 4). For the purpose of this discussion, hydrogen bonds between chloride ions and nearby hydrogen atoms are defined as those with distances of 2.6 Å or less,[115,125,126] whereas the term short contacts is used to refer to hydrogen bonds with distances of *ca.* 2.2 Å or less, based on earlier observations of their dominant influence on ^{35}Cl EFG tensors.[45] Although we have established relationships between ^{35}Cl EFG tensor parameters and the local environments of chlorine ions featuring one or two short contacts,[45] these relationships remain poorly understood for systems without short contacts, such as the urea MCCs, as well as for hydrates of organic HCl salts;[45,90] as such, continued exploration of these relationships is warranted.

The chloride ions in NEt$_4$Cl:2Urea feature four monodentate hydrogen bonds involving urea molecules. The largest principal component of the ^{35}Cl EFG tensor, V_{33}, is oriented near the bonding axis of the shortest hydrogen bond, $\angle$(H–Cl–V_{33}) = 19.3°, whereas V_{22} is oriented perpendicular to the pseudo-plane in which the chloride ion and four urea molecules reside.

By contrast, three of the four hydrogen bonds in NEt$_4$Cl:Urea·2H$_2$O involve water molecules, and a fourth involves urea. V_{33} resides between the second- and third-shortest hydrogen bonds with water molecules (*N.B.*: these water molecules are crystallographically equivalent through inversion symmetry). In both cases, the sign of C_Q is predicted to be negative (*i.e.*, V_{33} is positive since $Q(^{35}$Cl$) = -8.165$ fm^2).[45]

NPr$_4$Cl:2Urea has four H⋯Cl$^-$ hydrogen bonds, all of which are *ca.* 2.4 Å, stemming from bidentate interactions with two urea molecules, and resulting in a pyramidal Cl·(Urea)$_2^-$ structural unit. V_{33} is oriented perpendicular to the bonding axis with the shortest contact, $\angle$(H–Cl–V_{33}) = 99.4°, whereas V_{11} and V_{22} reside in the plane of the shortest contact

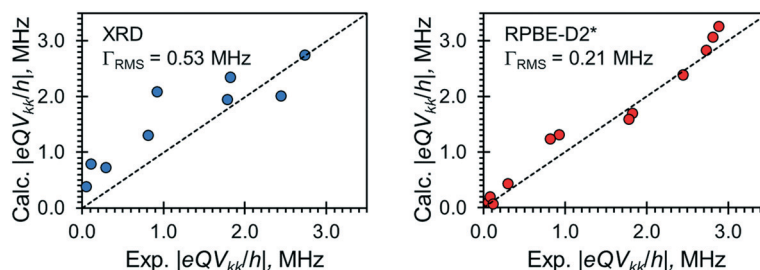**Fig. 3** Correlations between calculated and experimental principal components of ^{35}Cl EFG tensors for the four NR$_4$Cl:xUrea·yH$_2$O (R = Et, Pr; x = 1, 2, 3; y = 0, 1) MCCs. Computed EFG tensors are derived from calculations on the XRD-derived structures (blue) and structures with atomic coordinates refined at the RPBE-D2* level (red). Γ_{RMS} is the rms EFG distance, whereas the dotted lines represent prefect agreement between calculation and experiment.

Table 2 H···Cl⁻ contacts, contact angles, and calculated ^{35}Cl SSNMR parameters based on structural models refined at the RPBE-D2* level for all NR₄-Cl:xUrea·yH₂O materials discussed in this work

Material (Cl site)	Hydrogen bond type[a]	H···Cl⁻ distance[b] (Å)	X···Cl⁻ distance[c] (Å)	X–H···Cl⁻ angle[d] (°)	δ_{iso} (ppm)	C_Q (MHz)	η_Q
NEt₄Cl:2Urea	Urea···Cl⁻	2.318	3.276	173.2	85	−1.71	0.87
	Urea···Cl⁻	2.334	3.279	167.0			
	Urea···Cl⁻	2.378	3.328	169.4			
	Urea···Cl⁻	2.404	3.349	167.6			
NEt₄Cl:Urea·2H₂O	H₂O···Cl⁻	2.236	3.145	165.7	53	−3.27	0.88
	H₂O···Cl⁻	2.249	3.179	180.0			
	H₂O···Cl⁻	2.290	3.218	177.3			
	Urea···Cl⁻	2.498	3.453	173.4			
NPr₄Cl:2Urea	Urea···Cl⁻	2.415, 2.448	3.319, 3.345	156.9, 155.4	70	2.84	0.69
	Urea···Cl⁻	2.433, 2.499	3.332, 3.383	155.8, 153.1			
NPr₄Cl:3Urea	Urea···Cl⁻	2.402, 2.508	3.307, 3.381	157.4, 151.7	83	−1.32	0.89
	Urea···Cl⁻	2.441, 2.427	3.314, 3.320	155.1, 155.2			
	Urea···Cl⁻	2.451, 2.539	3.355, 3.424	157.3, 153.9			
NH₄Cl:Urea (Cl1)	NH₄⁺···Cl⁻	2.265	3.229	169.3	102	−3.33	0.53
	NH₄⁺···Cl⁻	2.265	3.229	169.3			
	Urea···Cl⁻	2.302	3.257	175.6			
	Urea···Cl⁻	2.319	3.270	172.3			
	Urea···Cl⁻	2.536, 2.536	3.420, 3.420	153.9, 153.9			
NH₄Cl:Urea (Cl2)	NH₄⁺···Cl⁻	2.259	3.230	173.3	91	4.63	0.34
	NH₄⁺···Cl⁻	2.259	3.230	173.3			
	Urea···Cl⁻	2.336	3.281	169.4			
	Urea···Cl⁻	2.336	3.281	169.4			
	Urea···Cl⁻	2.476, 2.548	3.369, 3.423	155.3, 152.5			

[a] The functional group involved in the H···Cl⁻ hydrogen bond (*e.g.*, H₂O···Cl⁻ signifies a hydrogen bond with a water molecule Urea···Cl⁻ signifies a hydrogen bond with a urea molecule, and NH₄⁺···Cl⁻ signifies a hydrogen bond with an ammonium cation). [b] Hydrogen bonds (<2.6 Å), as determined from crystal structures refined at the DFT-D2* level. Two distances are listed for bidentate hydrogen bonds with urea molecules. [c] Distance between the chloride ion and the hydrogen-bond donor atom (X = N, O). Two distances are listed for bidentate hydrogen bonds with urea molecules. [d] Angle between the hydrogen-bond donor atom (X = N, O), the hydrogen atom, and the chloride anion. Two angles are listed for bidentate hydrogen bonds with urea molecules.
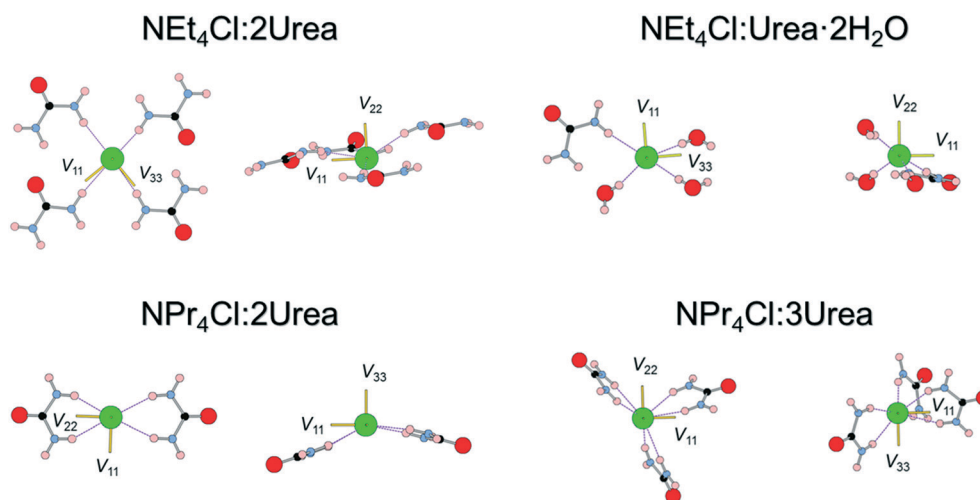
Fig. 4 ^{35}Cl EFG tensor orientations of all tetraethyl- and tetra(*n*-propyl)ammonium chloride MCCs obtained from model structures that were geometry optimized at the RPBE-D2* level. The H···Cl⁻ hydrogen bonds (<2.6 Å) are shown as dashed lines. The orientations of the three principal components of the EFG tensor (V_{11}, V_{22}, and V_{33}) are shown in yellow.

(*i.e.*, the EFGs are positive within this plane). The sign of C_Q is predicted to be positive (*i.e.*, V_{33} is negative), consistent with the orientation of V_{33} perpendicular to the shortest contacts.

Finally, the six hydrogen bonds in NPr₄Cl:3Urea, which range from 2.40–2.54 Å, involve bidentate interactions with three urea molecules, forming a paddlewheel configuration

about the chloride ion. For this chlorine site, which features the smallest value of C_Q for any of the MCCs, the orientation of the ^{35}Cl EFG tensor is not constrained by an apparent symmetry or pseudo-symmetry axis, and no simple relationships between tensor orientation or the sign of C_Q (predicted to be negative) are apparent.

In summary, this series of model structures featuring chloride ions with no short contacts reveals a number of interesting relationships between local structures and ^{35}Cl EFG tensor orientations, where in many instances, one or more principal components are found to align along or near key symmetry or pseudo-symmetry elements. Clearly, further investigations of more systems like these are likely to reveal EFG tensor-structure relationships that may greatly improve crystal structure prediction protocols.

Finally, the chlorine CS tensors for the four MCCs were calculated using the GIPAW approach (Fig. S12†). We find that refinement of the initial XRD-derived structures at the DFT-D2* level results in more accurate predictions of CS tensors than calculations on XRD-derived structures, which underestimate every principal component of the chlorine CS tensors, and are characterized by an RMS CS distance of Δ_{RMS} = 32 ppm (ESI† S3).[127] In contrast, calculations on the DFT-D2* refined structures do not feature this systematic error and are characterized by Δ_{RMS} = 11 ppm. Unlike the EFG tensors, there are apparently no straightforward relationships between the chlorine CS tensors and the types, numbers, and spatial arrangements of hydrogen bonds that can be drawn; however, there is potential for chlorine CS tensor parameters to be used as additional constraints in NMR crystallographic protocols.

3.3 NH$_4$Cl:Urea

NH$_4$Cl:Urea was synthesized using both crystallization from water (seven days to yield crystals suitable for analysis by SCXRD) and ball milling (10 minutes). Both preparations led to the formation of the same product, as indicated by their similar PXRD patterns; however, neither of these match the simulated PXRD patterns based on previously-reported crystal structures (Fig. S13†).[128–130] In particular, these simulations indicate the presence of several low angle reflections ($2\theta < 12°$) that are not detected in our experimental PXRD patterns. Single crystals of suitable size were grown for SCXRD analysis to determine if these differences arise from (i) an issue with the ball milling preparation method, (ii) production of a novel NH$_4$Cl:Urea form, and/or (iii) problems with the previously-reported crystal structures.[128–130]

Our new crystal structure of NH$_4$Cl:Urea crystallizes in the orthorhombic space group *Pmna*, with $Z' = 1$, $Z = 8$, unit cell parameters of a = 7.8835(4) Å, b = 17.0669(8) Å, and c = 8.0099(3) Å, and an asymmetric unit that has two crystallographically-distinct pairs of half molecules that are either bisected by a crystallographic C_2 symmetry axis or feature a mirror plane in the plane of the molecule (see Table S3† for details). The simulated PXRD patterns based on this crystal structure match the experimental patterns of the solids from mechanochemical synthesis and crystallization from water. Additionally, our *Pmna* solution was subjected to a plane-wave DFT-D2* geometry optimization and was found to have a static lattice energy that agrees to within 0.7 kJ mol^{-1} of the previously-reported *Pmna* structures.[129,130] A

calculation was also attempted on the previously-reported *Pcnm* structure,[128] though this did not converge.

The ^{35}Cl SSNMR spectra feature three underlying patterns: two broad second-order quadrupolar patterns and one narrow pattern (Fig. 5). The two broad patterns correspond to the two crystallographically and magnetically distinct chloride ions, which are characterized by C_Q = 3.52(5) MHz, η_Q = 0.14(8) and C_Q = 2.62(6) MHz, η_Q = 0.49(5), respectively (Table 3). An additional sharp feature located at δ_{iso} = 120(1) ppm corresponds to a trace amount of unreacted NH$_4$Cl, which is not detected in the corresponding PXRD patterns. There are three factors we consider in performing a quantitative Hahn echo NMR experiment on half-integer quadrupolar nuclei.[131] First, we ensure the dataset was acquired with a sufficiently long recycle delay (in this case, 1 s) to allow for complete return to equilibrium magnetization.[132] Second, we use CT-selective pulses, which result in uniform nutations of individual isochromats in the CT patterns, which ensures that integrated intensities can be regarded as quantitative.[133–135] Finally, the effective T_2's ($T_2^{eff}(^{35}$Cl)) for chloride ions in organic HCl salts are typically on the order of 2–20 ms; since an interpulse delay of 20 μs was used in the Hahn echo experiment, this has minor impact on the signal intensity collected after the refocusing pulse. Hence, we are able to reliably quantify not only the relative intensities of the two patterns corresponding to the chloride ions in the MCC (*i.e.*, ~1:1), but also the relative intensities of the patterns corresponding to NH$_4$Cl and MCC (*i.e.*, 2.5:97.5, or 1.9 ± 0.5 wt% NH$_4$Cl).

Unlike the other urea-containing MCCs, calculations of the ^{35}Cl EFG tensors of NH$_4$Cl:Urea do not result in good agreement with experimental values (Tables 3 and S6,† including calculations on geometry-optimized structural models based on our new crystal structure and those reported previously). The resulting EFG distances are large enough that no definitive assignment can be made for the two crystallographically distinct chloride ions. Their assignment is further complicated by the fact that both chloride ions have similar local environments (Fig. S14†), consisting of a bidentate hydrogen bond to one urea molecule, two monodentate hydrogen bonds with two additional urea molecules, and two hydrogen bonds with NH$_4^+$ ions; of these contacts, the hydrogen bonds to the NH$_4^+$ ions are the shortest (*ca.* 2.26 Å), and are therefore likely to exhibit the strongest influence on the calculated ^{35}Cl EFG tensors (see Fig. S14† for EFG tensor orientations).

To explore the influence of molecular-level dynamics on the observed ^{35}Cl EFG tensor parameters of NH$_4$Cl:Urea, we measured variable-temperature (VT) ^{35}Cl{^{1}H} spectra between 25 and −125 °C at 14.1 T (Fig. 6). At all temperatures, the narrower pattern is characterized by C_Q = 2.62(6) MHz and η_Q = 0.49(5) (*i.e.*, no observable change in the EFG tensor with temperature). For the broader pattern, C_Q increases from 3.52(5) MHz at 25 °C to 3.94(7) MHz at −125 °C, and the value of η_Q = 0.14(7) remains largely constant. The temperature-dependent variation of the ^{35}Cl EFG tensor
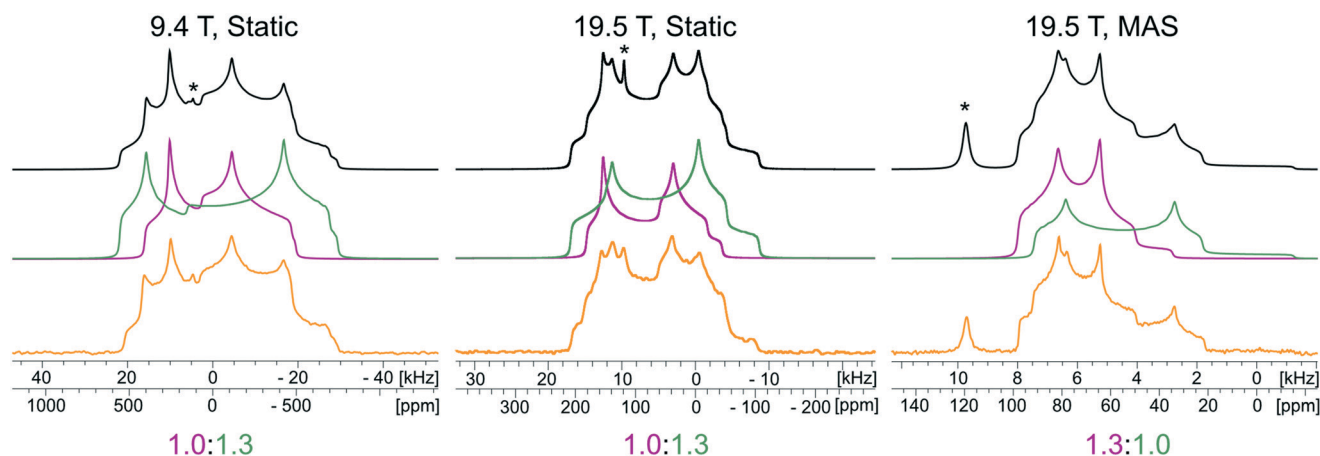
Fig. 5 Experimental $^{35}Cl\{^1H\}$ SSNMR spectra of NH_4Cl:Urea (lower traces), corresponding analytical simulations (upper traces), and deconvolutions of the simulations (middle traces). Spectra were acquired at two fields (B_0 = 9.4 T and 19.5 T) under static and MAS conditions (ν_{rot} = 16 kHz). Peaks corresponding to NH_4Cl educt are indicated with asterisks (*).

parameters of the broader pattern, and the fact that the crystal structure of NH_4Cl:Urea does not change substantially over the same temperature range (*i.e.*, the experimental unit cell volume increases by 1.6% at 298 K, relative to the structure at 170 K) suggest that molecular-level dynamics influence these values.

A growing body of work has demonstrated that certain NMR parameters are influenced by fast (femtosecond) time scale molecular-level motions that can be calculated using *ai*MD simulations;[136–141] these effects can be modelled by averaging NMR interaction tensors over a representative sample of "snapshot" structures taken from an *ai*MD simulation. For example, Dračínský and Hodgkinson report that the effects of fast MD (*i.e.*, vibrational motions, conformational averaging, molecular tumbling, *etc.*) can decrease the magnitudes of $C_Q(^{35}Cl)$ in HCl salts by as much as 0.4 MHz.[137] A similar analysis demonstrated that fast molecular motions have very little influence on the value of $C_Q(^{35}Cl)$ for glycine HCl, whereas the magnitude of $C_Q(^{35}Cl)$ in $NaClO_3$, an inorganic solid, is decreased by *ca.* 1.6 MHz.[140] Thus, it is possible that the poor agreement between

experimental and calculated values of the ^{35}Cl EFG tensors for the static structure of NH_4Cl:Urea could be corrected by a model that accounts for the effects of fast molecular dynamics in the DFT calculations.

The effects of fast molecular dynamics have a substantial influence on the calculated ^{35}Cl EFG tensor parameters of NH_4Cl:Urea (Table 3). For the crystallographic sites Cl1 and Cl2, the *ai*MD simulations carried out at 300 K yield values of C_Q = −3.98 MHz, η_Q = 0.23 and C_Q = 2.91 MHz, η_Q = 0.47, respectively (Fig. 7). A definitive assignment of the two chlorine sites can be made based on comparison of the ^{35}Cl EFG tensors measured at room temperature with those from *ai*MD simulations. The broader ^{35}Cl CT powder pattern corresponds to Cl1, whereas the narrower pattern corresponds to Cl2.

The motions of atoms in the vicinity of the chloride ions, especially those within the NH_4^+ ions, can have a substantial impact on the EFG tensors of the chloride ions – this hypothesis is further substantiated by calculations on the static DFT-D2* model of NH_4Cl:Urea, for which V_{33} is predicted to reside either perpendicular to the plane formed by the two nearest NH_4^+ ions (Cl1) or within the plane (Cl2). The *ai*MD calculations reveal significant molecular-level motions of these atoms, as can be elucidated by examining the distributions of H···Cl and N···Cl internuclear distances (Fig. 8). The *ai*MD time-averaged H···Cl and N···Cl interatomic distances are nearly identical to those in the static DFT-D2* structure (*i.e.*, these differences are less than 0.02 Å in all cases); however, the MD snapshot structures show large distributions for these distances. For both chloride ions, this analysis demonstrates that the motions of the NH_4^+ ions consist of two types: (i) vibrations of the ions around their equilibrium positions (indicated by the distribution of N···Cl distances), and (ii) random tumbling of the ions (indicated by the larger asymmetric distribution of H···Cl distances). Interestingly, the distribution of H···Cl distances for Cl2 is more heavily skewed toward longer bond

Table 3 Summary of the experimental (room temperature) and calculated ^{35}Cl EFG tensor parameters for the two chloride ions in NH_4Cl:Urea

Cl site		C_Q (MHz)	η_Q	Γ_{RMS} (MHz)^c
Cl1	Exp.	3.52(5)	0.14(8)	—
	Static Calc.^{a}	−3.33	0.53	0.35
	Dynamic Calc.^{b}	−3.98	0.23	0.33
Cl2	Exp.	2.62(6)	0.49(5)	—
	Static Calc.	4.63	0.34	1.37
	Dynamic Calc.	2.91	0.47	0.20

^{a} Static calculations refer to a structural model derived from the crystal structure that was refined at the DFT-D2* level. ^{b} Dynamic calculations refer to an ensemble of 400 "snapshot" structures taken from the *ai*MD simulations, using the DFT-D2* structure as a starting point. ^{c} Γ_m is the EFG distance for a single chlorine nucleus. See ESI† S2.
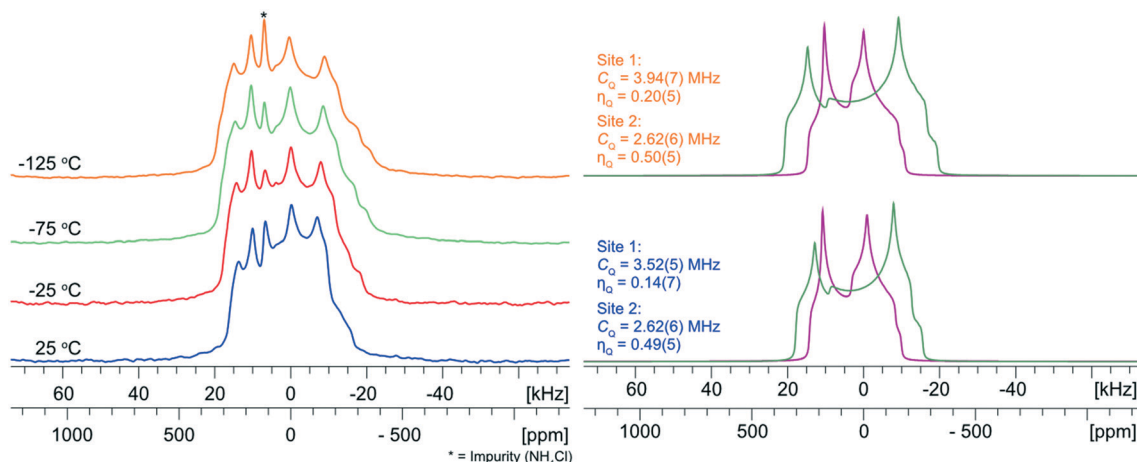
Fig. 6 Experimental ^{35}Cl{^{1}H} VT-NMR spectra of NH$_4$Cl:Urea from 25 to −125 °C. To the right are deconvolutions of the spectra acquired at 25 and −125 °C with corresponding ^{35}Cl EFG tensor parameters. For the narrow pattern (site 2) there is negligible change in the ^{35}Cl EFG tensor parameters. For the broad pattern (site 1), there is an increase in the value of C_Q with decreasing temperature, while the value of η_Q remains constant (within experimental uncertainty).
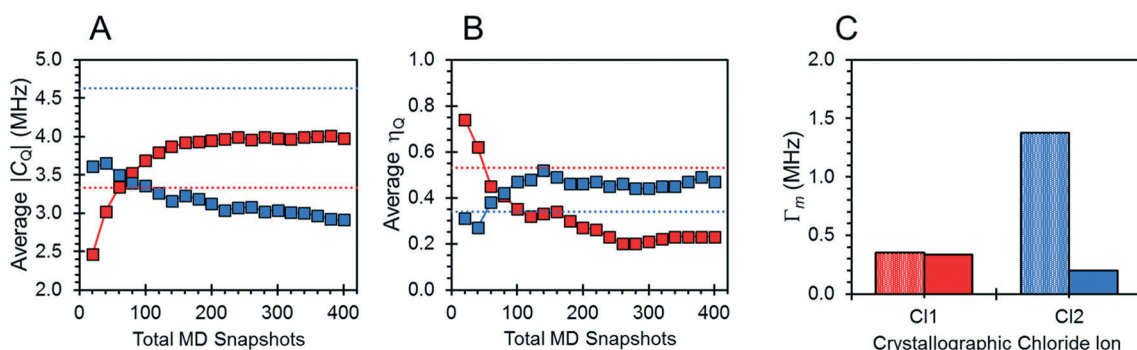

Fig. 7 (A and B) The convergence of the ^{35}Cl EFG tensor parameters for NH$_4$Cl:Urea with respect to the total number of *ai*MD snapshot structures (squares), as well as the EFG tensor parameters obtained from a calculation on a static energy-minimized structure (dotted red and blue lines). (C) EFG distances for the distinct crystallographic chloride ions. Values are illustrated for the distinct chloride ions, Cl1 (red) and Cl2 (blue).

lengths (*i.e.*, weaker hydrogen bonds), which is consistent with the lower value of C_Q observed for this site.

4. Conclusions

Herein, we have demonstrated novel mechanochemical preparations of five ammonium chloride urea MCCs, and their structural characterization by ^{35}Cl and ^{13}C SSNMR spectroscopy, PXRD and/or SCXRD, and plane-wave DFT calculations. These urea MCCs can be prepared mechanochemically with high purity and great rapidity, relative to crystallization from solution; this was confirmed using a combination of ^{35}Cl SSNMR and PXRD data to validate the products, identify any impurities and/or leftover starting material, and optimize the experimental conditions for ball milling. In combination with DFT calculations, ^{35}Cl EFG tensors can be used to validate and refine crystal structures, as well as to examine their relationship to structural features. *ai*MD simulations and VT-NMR indicate that the ^{35}Cl EFG tensors for NH$_4$Cl:Urea are significantly

affected by fast molecular-level motions, and careful attention must be paid to systems with mobile functional groups and/or counterions. Together, these methods could be beneficial for designing new quadrupolar-based NMR crystallography techniques to validate, refine, and solve the crystal structures of a wide range of MCCs where traditional characterization methods are difficult or impossible.

Finally, during the optimization of our ball milling routines, and the discovery of extremely short preparation times, we observed that the synthesis of certain ammonium chloride urea MCCs is possible with other green synthetic techniques, including accelerated aging.[142] Since accelerated aging reactions progress slower than ball milling reactions (*i.e.*, days *versus* minutes), they provide a unique opportunity to monitor reactions *in situ*, potentially allowing for the detection and identification of intermediate phases, and even providing a pathway for rational design of novel MCCs. Discussion of this exciting prospect is beyond the scope of this work, but explorations of these phenomena are already underway in our laboratory.
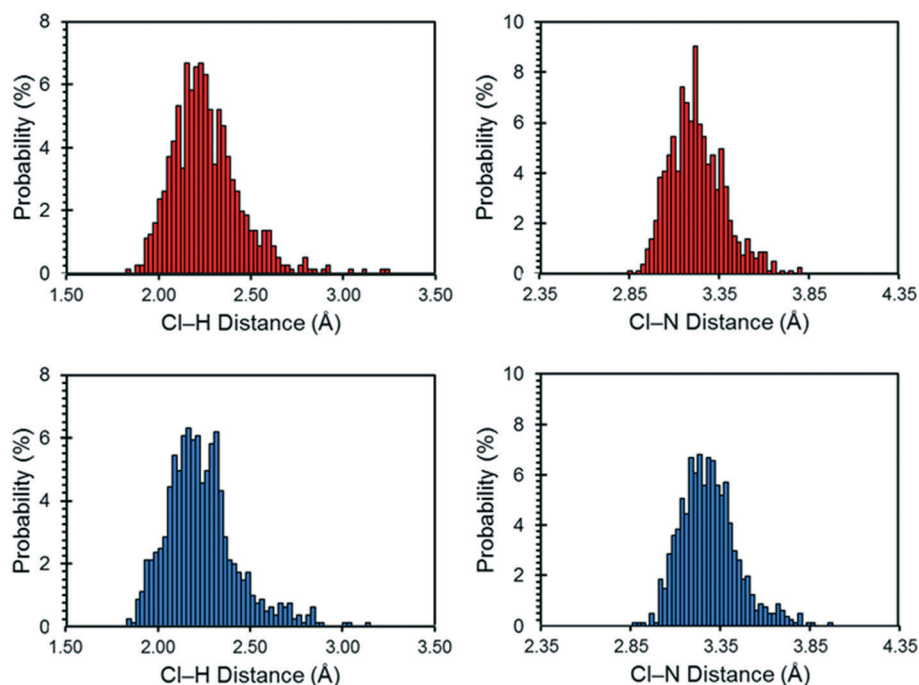
Fig. 8 Distribution of Cl⋯H and Cl⋯N distances (bin size of 0.025 Å) for NH$_4$Cl:Urea as determined by *ai*MD simulations conducted at 300 K. Results are shown for the crystallographic sites Cl1 (red) and Cl2 (blue).

Conflicts of interest

There are no conflicts to declare.

Acknowledgements

References

1 G. R. Desiraju, *J. Am. Chem. Soc.*, 2013, **135**, 9952–9967.

2 A. Karagianni, M. Malamatari and K. Kachrimanis, *Pharmaceutics*, 2018, **10**, 1–30.

3 R. Thakuria, A. Delori, W. Jones, M. P. Lipert, L. Roy and N. Rodríguez-Hornedo, *Int. J. Pharm.*, 2013, **453**, 101–125.

4 M. Karimi-Jafari, L. Padrela, G. M. Walker and D. M. Croker, *Cryst. Growth Des.*, 2018, **18**, 6370–6387.

5 T. Friščić and W. Jones, *J. Pharm. Pharmacol.*, 2010, **62**, 1547–1559.

6 D. P. McNamara, S. L. Childs, J. Giordano, A. Iarriccio, J. Cassidy, M. S. Shet, R. Mannion, E. O'Donnell and A. Park, *Pharm. Res.*, 2006, **23**, 1888–1897.

7 D. R. Weyna, T. Shattock, P. Vishweshwar and M. J. Zaworotko, *Cryst. Growth Des.*, 2009, **9**, 1106–1123.

8 G. Kuminek, F. Cao, A. B. O. da Rocha, S. G. Cardoso and N. Rodríguez-Hornedo, *Adv. Drug Delivery Rev.*, 2016, **101**, 143–166.

9 D. Tan and F. García, *Chem. Soc. Rev.*, 2019, **48**, 2274–2292.

10 J. L. Howard, Q. Cao and D. L. Browne, *Chem. Sci.*, 2018, **9**, 3080–3094.

11 T. Friščić, C. Mottillo and H. M. Titi, *Angew. Chem., Int. Ed.*, 2020, **59**, 1018–1029.

12 T. Friščić, *J. Mater. Chem.*, 2010, **20**, 7599.

13 D. Tan and T. Friščić, *Eur. J. Org. Chem.*, 2018, **2018**, 18–33.

14 D. Tan, L. Loots and T. Friščić, *Chem. Commun.*, 2016, **52**, 7760–7781.

15 J. Andersen and J. Mack, *Green Chem.*, 2018, **20**, 1435–1443.

16 S. L. James, C. J. Adams, C. Bolm, D. Braga, P. Collier, T. Friščic, F. Grepioni, K. D. M. Harris, G. Hyett, W. Jones, A. Krebs, J. Mack, L. Maini, A. G. Orpen, I. P. Parkin, W. C. Shearouse, J. W. Steed and D. C. Waddell, *Chem. Soc. Rev.*, 2012, **41**, 413–447.

17 R. B. N. Baig and R. S. Varma, *Chem. Soc. Rev.*, 2012, **41**, 1559–1584.

18 R. S. Varma, *Green Chem.*, 2014, **16**, 2027–2041.

19 E. Pindelska, A. Sokal and W. Kolodziejski, *Adv. Drug Delivery Rev.*, 2017, **117**, 111–146.

20 F. Taulelle, in *Encyclopedia of Magnetic Resonance*, ed. R. K. Harris, R. E. Wasylishen and M. J. Duer, John Wiley & Sons, Ltd, Chichester, UK, 2009, pp. 1–14.

21 R. E. Wasylishen, R. K. Harris and M. J. Duer, *NMR Crystallography*, A Wiley & Sons, New York, NY, 2009.

22 S. E. Ashbrook and D. McKay, *Chem. Commun.*, 2016, **52**, 7186–7204.

23 C. Martineau, *Solid State Nucl. Magn. Reson.*, 2014, **63–64**, 1–12.

24 P. Hodgkinson, *Prog. Nucl. Magn. Reson. Spectrosc.*, 2020, **118–119**, 10–53.

25 D. L. Bryce, *IUCrJ*, 2017, **4**, 350–359.

26 C. Leroy and D. L. Bryce, *Prog. Nucl. Magn. Reson. Spectrosc.*, 2018, **109**, 160–199.

27 C. Martineau, J. Senker and F. Taulelle, *NMR Crystallography*, 2014, vol. 82.

28 C. J. Pickard, *Nat. Rev. Mater.*, 2019, **4**, 331–348.

29 A. O. Lyakhov, A. R. Oganov and M. Valle, in *Modern Methods of Crystal Structure Prediction*, Wiley-VCH Verlag GmbH & Co. KGaA, Weinheim, Germany, 2010, pp. 147–180.

30 Ş. Atahan-Evrenk and A. Aspuru-Guzik, *Prediction and Calculation of Crystal Structures*, Springer International Publishing, Cham, 2014, vol. 345.

31 A. R. Oganov, G. Saleh and A. G. Kvashnin, *Computational Materials Discovery*, Royal Society of Chemistry, Cambridge, 2018.

32 C. M. Widdifield, J. D. Farrell, J. C. Cole, J. A. K. Howard and P. Hodgkinson, *Chem. Sci.*, 2020, **11**, 2987–2992.

33 J. R. Yates, S. E. Dobbins, C. J. Pickard, F. Mauri, P. Y. Ghi, R. K. Harris, L. D. M. De Paris, U. Pierre, P. Jussieu and C. Paris, *Methods*, 2005, 1402–1407.

34 T. Pawlak, M. Jaworska and M. J. Potrzebowski, *Phys. Chem. Chem. Phys.*, 2013, **15**, 3137–3145.

35 S. E. Soss, P. F. Flynn, R. J. Iuliucci, R. P. Young, L. J. Mueller, J. Hartman, G. J. O. Beran and J. K. Harper, *ChemPhysChem*, 2017, **18**, 2225–2232.

36 K. Kalakewich, R. Iuliucci, K. T. Mueller, H. Eloranta and J. K. Harper, *J. Chem. Phys.*, 2015, **143**, 194702.

37 A. Abraham, D. C. Apperley, T. Gelbrich, R. K. Harris and U. J. Griesser, *Can. J. Chem.*, 2011, **89**, 770–778.

38 A. E. Watts, K. Maruyoshi, C. E. Hughes, S. P. Brown and K. D. M. Harris, *Cryst. Growth Des.*, 2016, **16**, 1798–1804.

39 M. Baias, C. M. Widdifield, J.-N. Dumez, H. P. G. Thompson, T. G. Cooper, E. Salager, S. Bassil, R. S. Stein, A. Lesage, G. M. Day and L. Emsley, *Phys. Chem. Chem. Phys.*, 2013, **15**, 8069.

40 J. D. Hartman, G. M. Day and G. J. O. Beran, *Cryst. Growth Des.*, 2016, **16**, 6479–6493.

41 S. T. Holmes, O. G. Engl, M. N. Srnec, J. D. Madura, R. Quiñones, J. K. Harper, R. W. Schurko and R. J. Iuliucci, *J. Phys. Chem. A*, 2020, **124**, 3109–3119.

42 D. L. Bryce and G. D. Sward, *Magn. Reson. Chem.*, 2006, **44**, 409–450.

43 P. M. J. Szell and D. L. Bryce, in *Annual Reports on NMR Spectroscopy*, Elsevier Ltd., 1st edn, 2015, vol. 84, pp. 115–162.

44 Y. Xu, S. A. Southern, P. M. J. Szell and D. L. Bryce, *CrystEngComm*, 2016, **18**, 5236–5252.

45 M. Hildebrand, H. Hamaed, A. M. Namespetra, J. M. Donohue, R. Fu, I. Hung, Z. Gan and R. W. Schurko, *CrystEngComm*, 2014, **16**, 7334–7356.

46 K. M. N. Burgess, F. A. Perras, A. Lebrun, E. Messner-Henning, I. Korobkov and D. L. Bryce, *J. Pharm. Sci.*, 2012, **101**, 2930–2940.

47 D. L. Bryce, M. Gee and R. E. Wasylishen, *J. Phys. Chem. A*, 2001, **105**, 10413–10421.

48 R. W. Schurko and M. J. Jaroszewicz, in *Encyclopedia of Inorganic and Bioinorganic Chemistry*, John Wiley & Sons, Ltd, Chichester, UK, 2015, pp. 1–56.

49 I. L. Moudrakovski, in *Annual Reports on NMR Spectroscopy*, Elsevier Ltd., 1st edn., 2013, vol. 79, pp. 129–240.

50 G. Wu and J. Zhu, *Prog. Nucl. Magn. Reson. Spectrosc.*, 2012, **61**, 1–70.

51 S. T. Holmes, W. D. Wang, G. Hou, C. Dybowski, W. Wang and S. Bai, *Phys. Chem. Chem. Phys.*, 2019, **21**, 6319–6326.

52 K. M. N. Burgess, Y. Xu, M. C. Leclerc and D. L. Bryce, *Inorg. Chem.*, 2014, **53**, 552–561.

53 K. E. Johnston, J. M. Griffin, R. I. Walton, D. M. Dawson, P. Lightfoot and S. E. Ashbrook, *Phys. Chem. Chem. Phys.*, 2011, **13**, 7565.

54 S. Sene, B. Bouchevreau, C. Martineau, C. Gervais, C. Bonhomme, P. Gaveau, F. Mauri, S. Bégu, P. H. Mutin, M. E. Smith and D. Laurencin, *CrystEngComm*, 2013, **15**, 8763.

55 C. Bonhomme, C. Gervais, N. Folliet, F. Pourpoint, C. Coelho Diogo, J. Lao, E. Jallot, J. Lacroix, J. M. Nedelec, D. Iuga, J. V. Hanna, M. E. Smith, Y. Xiang, J. Du and D. Laurencin, *J. Am. Chem. Soc.*, 2012, **134**, 12611–12628.

56 H. Hamaed, J. M. Pawlowski, B. F. T. Cooper, R. Fu, S. H. Eichhorn and R. W. Schurko, *J. Am. Chem. Soc.*, 2008, **130**, 11056–11065.

57 S. T. Holmes, R. J. Iuliucci, K. T. Mueller and C. Dybowski, *J. Chem. Phys.*, 2017, **146**, 064201.

58 S. T. Holmes, C. S. Vojvodin and R. W. Schurko, *J. Phys. Chem. A*, 2020, **124**, 10312–10323.

59 A. A. Peach, D. A. Hirsh, S. T. Holmes and R. W. Schurko, *CrystEngComm*, 2018, **20**, 2780–2792.

60 C. M. Widdifield, F. A. Perras and D. L. Bryce, *Phys. Chem. Chem. Phys.*, 2015, **17**, 10118–10134.

61 C. Martineau, A. Cadiau, B. Bouchevreau, J. Senker, F. Taulelle and K. Adil, *Dalton Trans.*, 2012, **41**, 6232.

62 C. M. Rice, Z. H. Davis, D. McKay, G. P. M. Bignami, R. G. Chitac, D. M. Dawson, R. E. Morris and S. E. Ashbrook, *Phys. Chem. Chem. Phys.*, 2020, **22**, 14514–14526.

63 S. T. Holmes, J. M. Hook and R. W. Schurko, *Mol. Pharmaceutics*, 2022, **19**, 440–455.

64 D. A. Hirsh, S. T. Holmes, P. Chakravarty, A. A. Peach, A. G. Dipasquale, K. Nagapudi and R. W. Schurko, *Cryst. Growth Des.*, 2019, **19**, 7349–7362.

65 A. M. Namespetra, D. A. Hirsh, M. P. Hildebrand, A. R. Sandre, H. Hamaed, J. M. Rawson and R. W. Schurko, *CrystEngComm*, 2016, **18**, 6213–6232.

66 R. J. Attrell, C. M. Widdifield, I. Korobkov and D. L. Bryce, *Cryst. Growth Des.*, 2012, **12**, 1641–1653.

67 D. A. Hirsh, A. J. Rossini, L. Emsley and R. W. Schurko, *Phys. Chem. Chem. Phys.*, 2016, **18**, 1–34.

68 F. G. Vogt, G. R. Williams and R. C. B. Copley, *J. Pharm. Sci.*, 2013, **102**, 3705–3716.

69 D. L. Bryce, G. D. Sward and S. Adiga, *J. Am. Chem. Soc.*, 2006, **128**, 2121–2134.

70 B. Sandhu, A. S. Sinha, J. Desper and C. B. Aakeröy, *Chem. Commun.*, 2018, **54**, 4657–4660.

71 K. Honer, C. Pico and J. Baltrusaitis, *ACS Sustainable Chem. Eng.*, 2018, **6**, 4680–4687.

72 K. Honer, E. Kalfaoglu, C. Pico, J. McCann and J. Baltrusaitis, *ACS Sustainable Chem. Eng.*, 2017, **5**, 8546–8550.

73 L. Mazzei, V. Broll, L. Casali, M. Silva, D. Braga, F. Grepioni, J. Baltrusaitis and S. Ciurli, *ACS Sustainable Chem. Eng.*, 2019, **7**, 13369–13378.

74 P. Macfhionnghaile, C. M. Crowley, P. McArdle and A. Erxleben, *Cryst. Growth Des.*, 2020, **20**, 736–745.

75 L. Casali, L. Mazzei, O. Shemchuk, L. Sharma, K. Honer, F. Grepioni, S. Ciurli, D. Braga and J. Baltrusaitis, *ACS Sustainable Chem. Eng.*, 2019, **7**, 2852–2859.

76 P. A. Julien, L. S. Germann, H. M. Titi, M. Etter, R. E. Dinnebier, L. Sharma, J. Baltrusaitis and T. Friščić, *Chem. Sci.*, 2020, **11**, 2350–2355.

77 K. D. M. Harris and J. M. Thomas, *J. Chem. Soc., Faraday Trans.*, 1990, **86**, 2985–2996.

78 J. T. Zou, Y. S. Wang, W. M. Pang, L. Shi and F. Lu, *Chin. J. Chem. Phys.*, 2013, **26**, 198–202.

79 S. Thakral and A. K. Madan, *J. Inclusion Phenom. Macrocyclic Chem.*, 2008, **60**, 203–209.

80 I. J. Shannon, N. M. Stainton and K. D. M. Harris, *J. Mater. Chem.*, 1993, **3**, 1085–1090.

81 A. Alhalaweh, S. George, D. Boström and S. P. Velaga, *Cryst. Growth Des.*, 2010, **10**, 4847–4855.

82 L. Casali, L. Mazzei, O. Shemchuk, K. Honer, F. Grepioni, S. Ciurli, D. Braga and J. Baltrusaitis, *Chem. Commun.*, 2018, **54**, 7637–7640.

83 P. Cysewski, M. Przybyłek, D. Ziółkowska and K. Mroczyńska, *J. Mol. Model.*, 2016, **22**, 103.

84 J. X. Song, Y. Yan, J. Yao, J. M. Chen and T. B. Lu, *Cryst. Growth Des.*, 2014, **14**, 3069–3077.

85 S. T. Holmes and R. W. Schurko, *J. Phys. Chem. C*, 2018, **122**, 1809–1820.

86 Bruker, APEXIII, SAINT, SADABS, 2016, Madison, WI, USA.

87 G. M. Sheldrick, *Acta Crystallogr., Sect. A: Found. Adv.*, 2015, **71**, 3–8.

88 G. M. Sheldrick, *Acta Crystallogr., Sect. C: Struct. Chem.*, 2015, **71**, 3–8.

89 O. V. Dolomanov, L. J. Bourhis, R. J. Gildea, J. A. K. Howard and H. Puschmann, *J. Appl. Crystallogr.*, 2009, **42**, 339–341.

90 P. M. J. Szell and D. L. Bryce, *Recent advances in chlorine, bromine, and iodine solid-state NMR spectroscopy*, Elsevier Ltd., 1st edn, 2020, vol. 100.

91 Bruker, TopSpin Softw. Version 4.1, 2020, Ettlingen, Germany.

92 S. G. J. van Meerten, W. M. J. Franssen and A. P. M. Kentgens, *J. Magn. Reson.*, 2019, **301**, 56–66.

93 M. E. Rose, *Elementary Theory of Angular Momentum*, Wiley, New York, NY, 1957.

94 M. Mehring, *Principles of High Resolution NMR in Solids*, Springer Berlin Heidelberg, Berlin, Heidelberg, 1983.

95 S. Adiga, D. Aebi and D. L. Bryce, *Can. J. Chem.*, 2007, **85**, 496–505.

96 A. Pines, M. G. Gibby and J. S. Waugh, *Chem. Phys. Lett.*, 1972, **15**, 373–376.

97 E. O. Stejeskal and J. Schaefer, *J. Am. Chem. Soc.*, 1976, **98**, 1031–1032.

98 C. R. Morcombe and K. W. Zilm, *J. Magn. Reson.*, 2003, **162**, 479–486.

99 S. J. Clark, M. D. Segall, C. J. Pickard, P. J. Hasnip, M. I. J. Probert, K. Refson and M. C. Payne, *Z. Kristallogr. Cryst. Mater.*, 2005, **220**, 567–570.

100 B. Hammer, L. B. Hansen and J. K. Nørskov, *Phys. Rev. B: Condens. Matter Mater. Phys.*, 1999, **59**, 7413–7421.

101 J. R. Yates, C. J. Pickard and F. Mauri, *Phys. Rev. B: Condens. Matter Mater. Phys.*, 2007, **76**, 1–11.

102 S. Grimme, *J. Comput. Chem.*, 2006, **27**, 1787–1799.

103 B. G. Pfrommer, M. Côté, S. G. Louie and M. L. Cohen, *J. Comput. Phys.*, 1997, **131**, 233–240.

104 J. Moellmann and S. Grimme, *J. Phys. Chem. C*, 2014, **118**, 7615–7621.

105 H. J. Monkhorst and J. D. Pack, *Phys. Rev. B: Solid State*, 1976, **13**, 5188–5192.

106 M. C. Payne, M. P. Teter, D. C. Allan, T. A. Arias and J. D. Joannopoulos, *Rev. Mod. Phys.*, 1992, **64**, 1045–1097.

107 T. A. Arias, M. C. Payne and J. D. Joannopoulos, *Phys. Rev. Lett.*, 1992, **69**, 1077–1080.

108 D. Alfè, *Comput. Phys. Commun.*, 1999, **118**, 31–33.

109 B. Leimkuhler, E. Noorizadeh and F. Theil, *J. Stat. Phys.*, 2009, **135**, 261–277.

110 C. J. Pickard and F. Mauri, *Phys. Rev. B: Condens. Matter Mater. Phys.*, 2001, **63**, 245101.

111 A. P. M. Kentgens, *Geoderma*, 1997, **80**, 271–306.

112 J. W. Akitt and W. S. McDonald, *J. Magn. Reson.*, 1984, **58**, 401–412.

113 O. Knop, E. M. Palmer and R. W. Robinson, *Acta Crystallogr., Sect. A: Cryst. Phys., Diffr., Theor. Gen. Crystallogr.*, 1975, **31**, 19–31.

114 G. Bartlett and I. Langmuir, *J. Am. Chem. Soc.*, 1921, **43**, 84–91.

115 G. Desiraju and T. Steiner, *The Weak Hydrogen Bond*, Oxford University Press, 2001, vol. 9.

116 M. Light, C. Haynes and P. A. Gale, *CSD Commun.*, 2016.

117 Q. Li and T. C. W. Mak, *Acta Crystallogr., Sect. B: Struct. Sci.*, 1998, **54**, 180–192.

118 Q. Li, W. H. Yip and T. C. W. Mak, *J. Inclusion Phenom. Mol. Recognit. Chem.*, 1995, **23**, 233–244.

119 Q. Li and T. C. W. Mak, *J. Inclusion Phenom. Mol. Recognit. Chem.*, 1997, **28**, 151–161.

120 C. F. Holder and R. E. Schaak, *ACS Nano*, 2019, **13**, 7359–7365.

121 R. T. Berendt and E. J. Munson, *J. Pharm. Sci.*, 2011, **100**, 1879–1891.

122 K. D. M. Harris and J. M. Thomas, *J. Solid State Chem.*, 1991, **94**, 197–205.

123 D. V. Dudenko, P. A. Williams, C. E. Hughes, O. N. Antzutkin, S. P. Velaga, S. P. Brown and K. D. M. Harris, *J. Phys. Chem. C*, 2013, **117**, 12258–12265.

124 F. G. Vogt, J. S. Clawson, M. Strohmeier, A. J. Edwards, T. N. Pham and S. A. Watson, *Cryst. Growth Des.*, 2009, **9**, 921–937.

125 S. Thomas, *Angew. Chem., Int. Ed.*, 2002, **41**, 48–76.

126 T. Steiner, *Chem. Commun.*, 1999, 313–314.

127 D. W. Alderman, M. H. Sherwood and D. M. Grant, *J. Magn. Reson.*, 1993, **101**, 188–197.

128 A. Rimsky, *Bull. Soc. Fr. Mineral. Cristallogr.*, 1960, **83**, 187–200.

129 B. Xue, M. Mao, Y. Liu, J. Guo, J. Li and E. Liu, *J. Cryst. Growth*, 2016, **442**, 110–113.

130 Y. Wang, J. Han, A. Tudi, Z. Zhang, Z. Yang and S. Pan, *CrystEngComm*, 2019, **21**, 6072–6079.

131 D. A. Hirsh, Y. Su, H. Nie, W. Xu, D. Stueber, N. Variankaval and R. W. Schurko, *Mol. Pharmaceutics*, 2018, **15**, 4038–4048.

132 M. J. R. Hoch, S. P. McAlister and M. I. Gordon, *J. Phys. C: Solid State Phys.*, 1975, **8**, 53–70.

133 A. J. Vega, in *Encyclopedia of Magnetic Resonance*, ed. D. M. Grant and R. K. Harris, John Wiley & Sons, Ltd, Chichester, UK, 2010, pp. 3869–3888.

134 P. P. Man, J. Klinowski, A. Trokiner, H. Zanni and P. Papon, *Chem. Phys. Lett.*, 1988, **151**, 143–150.

135 A. Samoson and E. Lippmaa, *Phys. Rev. B*, 1983, **28**, 6567–6570.

136 M. Dračínský, H. M. Moller and T. E. Exner, *J. Chem. Theory Comput.*, 2013, **9**, 3806–3815.

137 M. Dračínský and P. Hodgkinson, *CrystEngComm*, 2013, **15**, 8705–8712.

138 M. Dračínský and P. Hodgkinson, *Chem. – Eur. J.*, 2014, **20**, 2201–2207.

139 M. Dračínský, P. Bour and P. Hodgkinson, *J. Chem. Theory Comput.*, 2016, **12**, 968–973.

140 O. Socha, P. Hodgkinson, C. M. Widdifield, J. R. Yates and M. Dračínský, *J. Phys. Chem. A*, 2017, **121**, 4103–4113.

141 M. Dračínský, J. Vícha, K. Bártová and P. Hodgkinson, *ChemPhysChem*, 2020, **21**, 2075–2083.

142 M. J. Cliffe, C. Mottillo, R. S. Stein, D. K. Bučar and T. Friščić, *Chem. Sci.*, 2012, **3**, 2495–2500.